



Research Signpost
37/661 (2), Fort P.O.
Trivandrum-695 023
Kerala, India

The Mechanics of Faulting: From Laboratory to Real Earthquakes, 2012: 93-124
ISBN: 978-81-308-0502-3 Editors: Andrea Bizzarri and Harsha S. Bhat

4. Numerical algorithms for earthquake rupture dynamic modeling

Luis A. Dalguer

Swiss Seismological Service, ETH Zurich, CH-8092, Switzerland

Abstract. Numerical models of dynamic fault rupture provide a convenient framework to investigate the physical processes involved in the fault rupture during earthquake and the corresponding ground motion. This kind of model usually idealizes the earthquake rupture as a dynamically running shear crack on a frictional interface embedded in a linearly elastic continuum. This idealization has proven to be a useful foundation for analyzing natural earthquakes. The problem basically incorporates conservation laws of continuum mechanics, constitutive behavior of rocks under interface sliding, and state of stress in the crust. The fault kinematics (slip), is determined dynamically as part of the solution itself, by solving the elastodynamic equation coupled to frictional sliding. Here we describe the numerical implementation of this problem in finite difference solvers, but easily can be adapted to the different classes of finite element methods. Two approaches of fault representation are formulated, first the so called traction at split-node (TSN) scheme in which explicitly incorporates the fault discontinuity at velocity (and/or displacement) nodes, and second the inelastic-zone scheme, so called stress glut (SG) method, in which approximate the fault-rupture conditions through inelastic increments to the stress components. Finally we develop numerical tests to shortly evaluate the numerical models as well as to analyze some rupture phenomena.

Introduction

The study of earthquake rupture using dynamic models has the potential for important contributions to understanding different aspects related to the earthquake mechanism and near source ground motion. The idealization that earthquake ruptures in a shear crack embedded in a linearly elastic continuum, propagating spontaneously under pre-defined conditions of initial stresses, and sliding under a constitutive friction law, is a useful model for analyzing natural earthquake (e.g., [1,2,3,4,5,6,7,8,9,10,11,12,13]). This model leads to nonlinear, mixed boundary value problems. The nonlinearity occurs because the respective domains of the kinematic and dynamic boundary conditions are time dependent, and these domains have to be determined dynamically as part of the solution itself. The theoretical study of this problem class is usually possible only with computationally intensive numerical methods that solve the elastodynamic equations of motion in the continuum, coupling them to additional equations governing frictional sliding on the boundary representing the fault surface.

Suitable numerical solution techniques for the spontaneous rupture problem can be built into elastodynamic methods based upon, for example, finite difference (FD), finite element (FE), spectral element (SE), Discontinuous Galerkin (DG) or boundary integral (BI) methods. Each of these numerical methods can be implemented on any of several different grid types, and the elastodynamic equations solved to any specified order of accuracy. However, recent work by [14,15,16] has shown, at least in the case of the most widely used FD-based methods, that solution accuracy is controlled principally by the numerical formulation of the jump conditions on the fault discontinuity. In that study, as stated in [16], neither grid type nor order of spatial differencing in the grid is found to have a significant effect on spontaneous-rupture solution accuracy, but the method of approximation of the jump conditions has a very large effect. It is likely that a similar conclusion will hold for other solution methods such as the different classes of FE [16].

Here we compile some parts of our series of papers [14,15,16] to describe and evaluate the applications of two of the well known fault representation methods: 1) the so called traction-at-split-node (TSN) methods, and 2) the “inelastic-zone” stress glut (SG) method.

The TSN Methods represent the fault discontinuity by explicitly incorporating discontinuity terms at velocity and/or displacement nodes in the grid. It is the most widely used in different type of volumetric numerical methods, such as in the different classes of FD (e.g: [1,17,4, 14,15,16,17,18,19]), In FE methods (e.g. [20,21,22,23,24,25,26]) in SE

methods (e.g. 27,28,29)]. In the TSN method, interactions between the halves of the “split nodes” occur exclusively through the tractions (frictional resistance and normal traction) acting between them, and they in turn are controlled by the jump conditions and a friction law. This method permits a partition of the equations of motion into separate parts governing each side of the fault surface [14,16].

The SG method, a class of “inelastic-zone” models [15], introduced by [1,17], represents the fault discontinuity through inelastic increments to stress components at a set of stress grid points taken to lie on the fault plane. With this type of scheme, the fault surface is indistinguishable from an inelastic zone with a thickness given by the spatial step Δx (or an integral multiple of Δx). The SG methods are very easy to implement in FD codes, as no modification to the difference equations is required, only modifications to the way stress is calculated from strain rate. However, from the study of [15], in which the different classes of fault representation methods in FD schemes have been evaluated, the SG method is less accurate than the TSN formulation. In a 3D test, as shown by [15], the SG inelastic-zone method achieved solutions that are qualitatively meaningful and quantitatively reliable to within a few percent, but full convergence is uncertain, and SG proved to be less efficient computationally, relative to the TSN approach.

For academic purpose, in appendix, we provide a matlab script attached to a formulation of the TSN method implemented in a FD 1D elastodynamic equation. This matlab script is intended to introduce the reader to a conceptual implementation of the TSN in a numerical code.

Theoretical formulation of the problem

The problem is formulated assuming an isotropic, linearly elastic infinite space containing a fault surface Σ across which the displacement vector may have a discontinuity (Figure 1).

Assuming that surface Σ is parallel to the x - y plane, that is, perpendicular to the z axis, the linearized elastodynamics equations of the continuous media surrounding the fault surface Σ is represented, in its velocity-stress form, as:

$$\rho \frac{\partial \dot{u}_x}{\partial t} = \frac{\partial \sigma_{xx}}{\partial x} + \frac{\partial \tau_{xy}}{\partial y} + \frac{\partial \tau_{xz}}{\partial z} \quad (1a)$$

$$\rho \frac{\partial \dot{u}_y}{\partial t} = \frac{\partial \tau_{xy}}{\partial x} + \frac{\partial \sigma_{yy}}{\partial y} + \frac{\partial \tau_{yz}}{\partial z} \quad (1b)$$

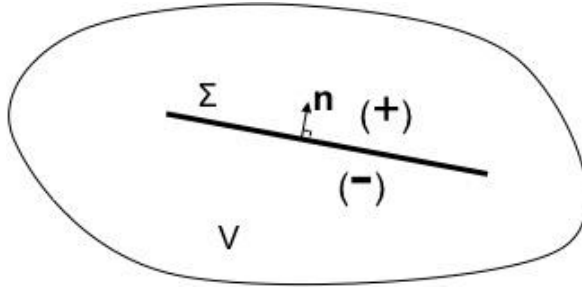


Figure 1. Schematic representation of a space of volume V containing a fault surface Σ with normal unit vector \mathbf{n} directed from negative side toward positive side of the fault.

$$\rho \frac{\partial \dot{u}_z}{\partial t} = \frac{\partial \tau_{xz}}{\partial x} + \frac{\partial \tau_{yz}}{\partial y} + \frac{\partial \sigma_{zz}}{\partial z} \quad (1c)$$

and the constitutive law (Hooke's law) as:

$$\frac{\partial \sigma_{xx}}{\partial t} = (\lambda + 2\mu) \frac{\partial \dot{u}_x}{\partial x} + \lambda \left(\frac{\partial \dot{u}_y}{\partial y} + \frac{\partial \dot{u}_z}{\partial z} \right), \quad (2a)$$

$$\frac{\partial \sigma_{yy}}{\partial t} = (\lambda + 2\mu) \frac{\partial \dot{u}_y}{\partial y} + \lambda \left(\frac{\partial \dot{u}_x}{\partial x} + \frac{\partial \dot{u}_z}{\partial z} \right), \quad (2b)$$

$$\frac{\partial \sigma_{zz}}{\partial t} = (\lambda + 2\mu) \frac{\partial \dot{u}_z}{\partial z} + \lambda \left(\frac{\partial \dot{u}_x}{\partial x} + \frac{\partial \dot{u}_y}{\partial y} \right), \quad (2c)$$

$$\frac{\partial \tau_{xy}}{\partial t} = \mu \left(\frac{\partial \dot{u}_y}{\partial x} + \frac{\partial \dot{u}_x}{\partial y} \right), \quad (2d)$$

$$\frac{\partial \tau_{xz}}{\partial t} = \mu \left(\frac{\partial \dot{u}_z}{\partial x} + \frac{\partial \dot{u}_x}{\partial z} \right), \quad (2e)$$

$$\frac{\partial \tau_{yz}}{\partial t} = \mu \left(\frac{\partial \dot{u}_z}{\partial y} + \frac{\partial \dot{u}_y}{\partial z} \right), \quad (2f)$$

Parameters λ and μ are the Lamé constants, ρ is density, $\dot{u} = \partial u / \partial t$ is the particle velocity formulated as the time derivative of the displacement u , σ is

the normal stress and τ is the shear stress. The fault surface Σ has a (continuous) unit normal vector \mathbf{n} . In our simple problem statement, in which no geometrical fault complexities are considered, this unit normal vector is always parallel to the axis z and directed toward the positive axis of z . A discontinuity in the displacement is permitted across the interface Σ . On Σ we define negative and positive sides of the fault surface such that \mathbf{n} (z axis) is directed from the former toward the latter. Taken Σ to be the plane $z=0$, the limiting values of the displacement vector, u_v^+ and u_v^- , is

$$u_v^\pm(v, z=0, t) = \lim_{\varepsilon \rightarrow 0} u_v(v, z = \pm\varepsilon, t), \quad \varepsilon > 0 \quad (3)$$

The superscripts (+) and (-) denote, respectively, the plus-side and minus-side of the fault plane (Figure 1); v indicates the vector components x, y tangential to the fault or z normal to the fault. Then the slip vector, defined as the discontinuity of the vector of tangential displacement of the positive side relative to the negative side, is given by ($v=x, y$)

$$s_v(t) = u_v^+(t) - u_v^-(t) \quad (4)$$

and its time derivative (slip rate) is denoted by $\dot{\mathbf{s}}$. The magnitude of the slip and slip rate are denoted, respectively, by $|s|$ and $|\dot{\mathbf{s}}|$. The open fault displacement ($v=z$) is formulated later.

The total shear traction vector (\mathbf{T}) acting on the fault ($z=0$) that is continuous across Σ with components $T_x = \tau_{xz}^0 + \Delta\tau_{xz}$ and $T_y = \tau_{yz}^0 + \Delta\tau_{yz}$ has its magnitude

$$|T| = \sqrt{T_x^2 + T_y^2} \quad (5)$$

where $\Delta\tau$ and τ^0 are, respectively, the shear stress change during rupture and initial shear stress.

As formulated in [14, 15, 16], the jump (rupture) conditions at the interface is given by

$$\tau_c - |T| \geq 0 \quad (6a)$$

$$\tau_c \dot{\mathbf{s}} - \mathbf{T} |\dot{\mathbf{s}}| = 0 \quad (6b)$$

Equation (6a) stipulates that the total shear traction T is bounded by a nonnegative frictional strength τ_c , and equation (6b) stipulates that any

nonzero velocity discontinuity be opposed by an antiparallel traction (i.e., the negative side exerts traction $-T$ on the positive side) with magnitude equal to the frictional strength τ_c . The frictional strength evolves according to some specified friction law

$$\tau_c = f(\sigma_n, s, \dot{s}, \varphi_1, \varphi_2, \dots) \quad (7)$$

that may depends on normal stress (σ_n), slip (s), slip rate (\dot{s}), and other mechanical or thermal variables ($\varphi_1, \varphi_2, \dots$).

Jump conditions (6a)–(6b), combined with the friction law (7) and appropriate initial stress conditions on Σ , provide a model of fault behavior. Under these conditions alone can model initial rupture, arrest of sliding and reactivation of slip.

When normal stress fluctuations are presents, the fault interface may undergo separation (fault opening) over portions of the contact surface Σ if there is a transient reduction of the compressive normal stress to zero [30,31]. For the sake of completeness, as formulated by [14], we describe an extension of the set of jump conditions appropriate to also incorporate fault opening due to normal stress fluctuations. We denote the normal component of the displacement discontinuity on Σ by U_n (fault opening displacement). From Equation 3, for $v=z$, the fault opening is given by

$$U_n(t) = u_z^+(t) - u_z^-(t) \quad (8)$$

The opening conditions, assuming negative normal stress in compression are

$$\sigma_n \leq 0, \quad (9a)$$

$$U_n \geq 0, \quad (9b)$$

$$\sigma_n U_n = 0 \quad (9c)$$

σ_n is the total normal stress acting on the fault that is given by $\sigma_n = \sigma_{zz}^0 + \Delta\sigma_{zz}$ where $\Delta\sigma$ and σ^0 are, respectively, the normal stress change during rupture and initial normal stress.

Equation (9a) bounds the total normal stress by the condition that tensile normal stress is not permitted; equation (9b) guarantees no interpenetration; and equation (9c) stipulate that loss of contact is permitted only if accompanied by zero normal stress. Again, these jump conditions are adequate to cover multiple episodes of tensile rupture and crack closure.

Traction-at-split-node (TSN) fault representation formulation

The TSN boundary formulation treats the fault rupture as a true contact problem between two surfaces in which the kinematic shear discontinuity (slip) as well as the open discontinuity (fault opening) are explicitly modeled. This method (for shear discontinuity) was reviewed by [17] and described the formulation in detail by [14,15,16] for implementation in finite difference schemes. Dalguer and Day [16] adapted it for a fourth-order velocity-stress staggered finite difference code. Here we give a general description of the method following [14,15].

We position the fault on the x-y plane. As shown in Figure 2, a given fault-plane node is split into plus-side and minus-side parts, with respective lumped nodal masses M^+ and M^- . The separate contributions from each side

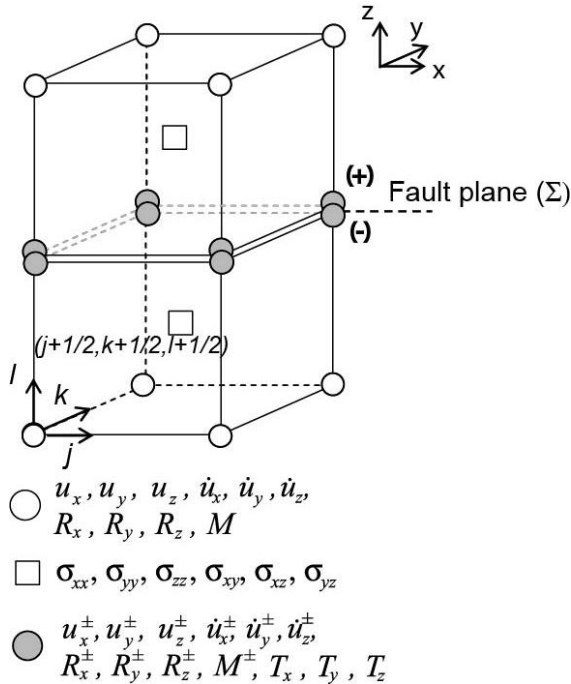


Figure 2. Traction at split node (TSN) fault representation method in a partially staggered cubic elements. Mass (M^\pm) is split, and separate elastic restoring forces (R_v^\pm) act on the two halves. The two halves of a split node interact only through shear and normal tractions (T_i) at the interface.

of the fault due to deformation of neighboring elements produce elastic restoring forces (nodal forces), R^+ and R^- . At a particular time (t), D'Alembert's principle leads to a nodal equilibrium equation of motion for each split node. At each step of integration the equation is solved by the central FD scheme to estimate the vector components of velocity (\dot{u}_v^\pm) and displacement (u_v^\pm) at a given node,

$$\dot{u}_v^\pm(t + \Delta t/2) = \dot{u}_v^\pm(t - \Delta t/2) + \frac{\Delta t}{M^\pm} \left\{ R_v^\pm(t) \mp a [T_v(t) - T_v^0] \right\} \quad (10a)$$

$$u_v^\pm(t + \Delta t) = u_v^\pm(t) + \Delta t \dot{u}_v^\pm(t + \Delta t/2) \quad (10b)$$

where v indicates the vector components x , y tangential to the fault or z normal to the fault, Δt is the time step, a is the area of the fault surface associated with each split node, T_v is the nodal value of the traction-vector components, and T_v^0 is the corresponding initial equilibrium value. The slip and slip velocity vectors (for $v = x$ or y) are then

$$s_v(t) = u_v^+(t) - u_v^-(t) \quad (11a)$$

$$\dot{s}_v(t + \Delta t/2) = \dot{u}_v^+(t + \Delta t/2) - \dot{u}_v^-(t + \Delta t/2) \quad (11b)$$

and fault opening displacement and velocity (making $v = z$)

$$U_n(t) = u_z^+(t) - u_z^-(t) \quad (12a)$$

$$\dot{U}_n(t + \Delta t/2) = \dot{u}_z^+(t + \Delta t/2) - \dot{u}_z^-(t + \Delta t/2) \quad (12b)$$

To find the slip, slip velocity and fault opening displacement we need to solve equation 10 by evaluating T_v as follow.

Evaluation of T_v for shear traction (kinematic fault tangential discontinuity)

An appropriate methodology is defining a trial traction vector \tilde{T}_v that would be required to enforce continuity of tangential velocity ($\dot{u}_v^+ - \dot{u}_v^- = 0$ for v equal to x and y) in equation (10a). The expression for \tilde{T}_v is then estimated after few operations in equations 10-11 [14,15,16]

$$\tilde{T}_v \equiv \frac{\Delta t^{-1} M^+ M^- (\dot{u}_v^+ - \dot{u}_v^-) + M^- R_v^+ - M^+ R_v^-}{a(M^+ + M^-)} + T_v^0, \quad v = x, y \quad (13)$$

where the velocities are evaluated at $t-\Delta t/2$, and the nodal tractions, restoring forces, and displacements are evaluated at t . The fault-rupture conditions stated in equations (6a,b) are satisfied if the fault-plane traction T_v of equation (10a) is

$$T_v = \begin{cases} \tilde{T}_v & \text{for } \left[(\tilde{T}_x)^2 + (\tilde{T}_y)^2 \right]^{1/2} \leq \tau_c \\ \tau_c \frac{\tilde{T}_v}{\left[(\tilde{T}_x)^2 + (\tilde{T}_y)^2 \right]^{1/2}} & \text{for } \left[(\tilde{T}_x)^2 + (\tilde{T}_y)^2 \right]^{1/2} > \tau_c \end{cases} \quad (14)$$

for $v = x, y$.

Evaluation of T_v for normal traction (kinematic fault normal discontinuity)

The same way as before, a trial fault normal traction \tilde{T}_z (making $v=z$) that would be required to enforce continuity of normal displacement ($u_z^+ - u_z^- = 0$) in (10b) is estimated. After some operations in equations 10 and 12 the expression of \tilde{T}_z is given by

$$\tilde{T}_z \equiv \frac{\Delta t^{-1} M^+ M^- (\dot{U}_n^{t-\Delta t/2} + \Delta t^{-1} U_n^t) + M^- R_z^+ - M^+ R_z^-}{a(M^+ + M^-)} + T_z^0 \quad (15)$$

where $\dot{U}_n^{t-\Delta t/2}$ is the fault opening velocity estimated at $t-\Delta t/2$ and U_n^t is the fault opening displacement estimated at t calculated using eq. (12). Assuming negative normal stress in compression and satisfying fault open conditions stated in equations (9), the fault normal traction T_z of equation 10a is

$$T_z = \begin{cases} \tilde{T}_z & \text{for } \tilde{T}_z \leq 0 \\ 0 & \text{for } \tilde{T}_z > 0 \end{cases} \quad (16)$$

The conditions in (16) guarantee no interpenetration and nontensile normal stress (i.e. the fault resistant to tensile is zero), consequently loss of contact between the two surface of the fault (opening) occurs only if accompanied by zero normal stress. This open fault boundary condition is rather simplified approximation, since the fault opening may follow a pre- process in which a certain amount of tensile stress may be admitted to break the contact between the two surfaces of the fault, but this pre-process is ignored here.

Stress glut (SG) “inelastic-zone” fault representation formulation

The SG method has been documented by [1,17] and adapted to a fourth-order velocity-stress staggered finite difference scheme by [15]. Considering the same grid element features in which the TSN formulation has been implemented above (Figure 2), the principal difference between the TSN method and the SG formulation is that the latter does not split the nodes neither place velocity nodes on the fault, but instead positions the fault to coincide with the standard grid points already containing the fault plane traction components (Figure 3). The fault discontinuity is not explicitly incorporated, rather it is represented through inelastic increments to those traction components. As

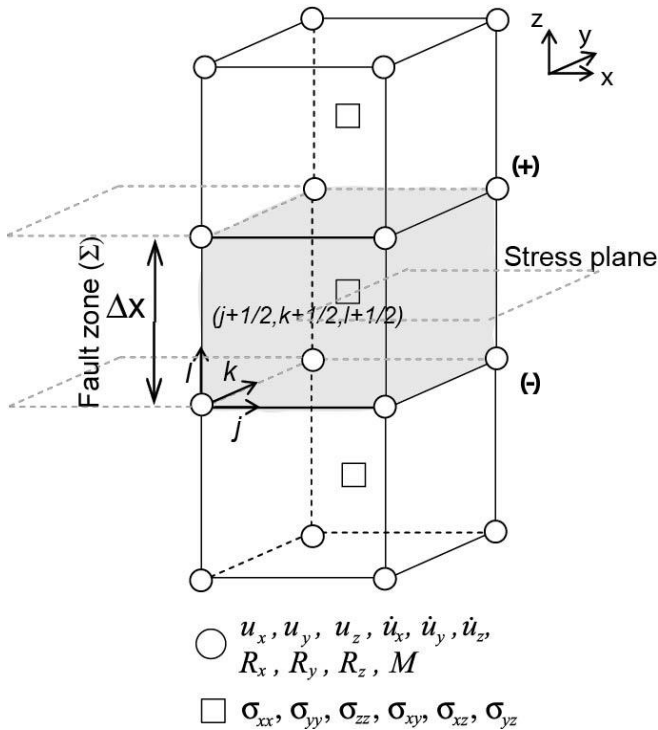


Figure 3. Inelastic-zone Stress glut (SG) fault representation method in a partially staggered cubic elements. The shear and normal tractions (T_v) acting on the fault are approximated by modifying the shearstress components located along the plane coinciding with the fault (labeled “stress plane”). This is equivalent to an inelastic zone of one grid-step (Δx) thickness.

shown in Figure 3, this formulation makes the fault indistinguishable from an inelastic zone of thickness Δx , where Δx is the dimension of the unit cell (assumed equal in all three coordinate directions for simplicity) of the grid. Due to this fault configuration, the fault normal discontinuity (fault opening) is also not explicit. So for this case, here we do not formulate fault opening boundary condition, and we limit our formulation to shear faulting boundary condition.

Here we reproduce the formulation stated in [15]. We again take the x - y plane as the fault surface. In the split-node method, we introduced extra grid variables T_x and T_y on the fault to represent the traction-vector components at the split nodes. In the SG method, no extra tractions have to be introduced to accommodate the fault; the faultplane traction components are located at the standard grid points for the tensor components σ_{xz} and σ_{yz} , respectively. However, we continue to use T_x and T_y to denote these two shear-traction components when they are located on the fault, for notational consistency with the split-node discussion.

Using the velocity-stress formulation of the equation of motion (Eq. 1 and 2), lets update nodal stresses assuming central differencing in time by using strain rates calculated from nodal velocities at $t-\Delta t/2$. Then, the shear stress components at a particular point acting on the fault plane take the form

$$\sigma_{vz}(t) = \sigma_{vz}(t - \Delta t) + \Delta t 2\mu \dot{\epsilon}_{vz}(t - \Delta t/2) \quad (17)$$

where v indicates the vector components x , y tangential to the fault, $\dot{\epsilon}_{vz}(t - \Delta t/2)$ is the strain rate and μ is the shear modulus. To implement the SG method, we modify this stress update scheme when calculating fault-plane traction components $T_v(t)$ by the addition of an inelastic component ($\dot{\epsilon}_{vz}^p$) to the total strain rate:

$$T_v(t) = T_v(t - \Delta t) + \Delta t 2\mu \left[\dot{\epsilon}_{vz}(t - \Delta t/2) - \dot{\epsilon}_{vz}^p(t - \Delta t/2) \right] \quad (18)$$

Then, as proceeded for the TSN method, lets calculate a trial traction, $\tilde{T}_v(t)$, that would be required to enforce zero inelastic strain rate, i.e.,

$$\tilde{T}_v(t) = T_v(t - \Delta t) + \Delta t 2\mu \dot{\epsilon}_{vz}(t - \Delta t/2) \quad (19)$$

Then the fault-plane traction $T_v(t)$ that satisfy fault-rupture conditions stated in equations (6) is calculated using eq. (14). The inelastic strain rate $\dot{\epsilon}_{vz}^p$ is estimated after some operations between equation (14), (18) and (19)

$$\dot{\varepsilon}_{vz}^p(t - \Delta t/2) = \frac{\tilde{T}_v(t) - T_v(t)}{2\mu\Delta t} \quad (20)$$

Fault slip is estimated through inelastic increments distributed in an inelastic zone of thickness Δx . Then the total slip rate on the fault is calculated by integrating the inelastic strain rate over the spatial step Δx in the direction normal to the fault, which gives

$$\dot{s}_v(t - \Delta t/2) = 2\Delta x \dot{\varepsilon}_{vz}^p(t - \Delta t/2) \quad (21)$$

from which the slip is then updated by central differencing,

$$s_v(t) = s_v(t - \Delta t) + \Delta t \dot{s}_v(t - \Delta t/2) \quad (22)$$

Frictional shear strength: Slip weakening friction model

As described in Eq. (7), the frictional shear strength τ_c in its general form evolves according to some specified friction law, and may depend upon normal stress, slip, slip velocity, and other mechanical or thermal variables. For simplicity, here we use the simple slip-weakening friction model in the form given by [1,2]. This friction law, first proposed by [32,33] by analogy to cohesive zone models of tensile fracture, is extensively used for shear dynamic rupture simulations (e.g. [1,2,4,6,34,35,36,37,8]).

The frictional strength τ_c is assumed to be proportional to normal stress σ_n (taken negative in compression)

$$\tau_c = -\mu_f \sigma_n \quad (23)$$

The coefficient of friction μ_f depends on the slip path length through the linear slip-weakening relationship [2]

$$\mu_f = \begin{cases} \mu_s - (\mu_s - \mu_d)|s|/d_0 & \text{for } |s| < d_0 \\ \mu_d & \text{for } |s| \geq d_0 \end{cases} \quad (24)$$

where μ_s and μ_d are coefficients of static and dynamic friction, respectively, d_0 is the critical slip-weakening distance, and $|s|$ is the magnitude of the slip vector.

Despite its limitations of the slip weakening model as a model for natural earthquakes (as noted in, e.g., [14], this friction law provides a suitable starting point for testing numerical methods. Other friction models are out of the scope of this chapter, in which interface frictional properties may be

better represented by more complicated relationships that account for rate and state effects (e.g. [38,39]) and thermal phenomena such as flash heating and pore pressure evolution (e.g., [40,41,42,43]).

Cohesive zone

The cohesive zone (Figure 4a) is the portion of the fault plane behind the crack tip where the shear stress decreases from its static value to its dynamic value and slip $|s|$ satisfies $0 < |s| < d_0$ (e.g. [32]). The cohesive model was first introduced by [44] in which constant cohesive zone was considered. Subsequently [32,33] proposed a cohesive zone model linearly dependent on distance to the crack tip; and Andrews [2] proposed a model linearly dependent on slip. Basically the models of [2,32,33] are equivalent and well known as slip-weakening model as formulated above. In this friction model, the cohesive zone, as shown in Figure 4a, examines the crack tip phenomena at a level of observation, in which the fracture energy G_c , (Figure 4b) is a mesoscopic parameter which contains all the dissipative processes in the volume around the crack tip, such as off-fault yielding, damage, micro-cracking etc. In the event that the normal stress and frictional parameters are constant over the entire fault, as will be the case in the test problem considered later, this idealized model results in constant fracture energy G_c with

$$G_c = (\tau_s - \tau_d)d_0/2 \tag{25}$$

where τ_s and τ_d are, respectively, the peak shear stress (static yielding stress) and dynamic yielding stress, given by

$$\tau_s = \mu_s |\sigma_n| \tag{26}$$

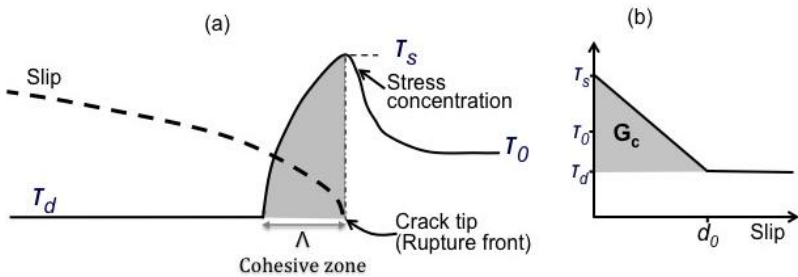


Figure 4. (a) Schematic representation of stress and slip along a shear crack and cohesive zone for a slip-weakening crack; (b) Stress-slip relationship of a slip-weakening model [2] and fracture energy G_c representation.

$$\tau_d = \mu_d |\sigma_n| \quad (27)$$

Note that in this context, the fracture energy G_c is not the surface energy defined by Griffith [45] in linear elastic fracture mechanics.

In the cohesive zone, shear stress and slip rate vary significantly, and proper numerical resolution of those changes is crucial for capturing the maximum slip rates and the rupture propagation time and speeds. Therefore an estimate of the cohesive zone width to calibrate numerical resolution would be useful. A review of some concepts of linear fracture mechanics and simple estimates for the cohesive zone size in two-dimensional cases of mode II and mode III was presented by [14]. These authors provide two ways to estimate the cohesive zone size and calibrate numerical resolution: the zero-speed cohesive zone width Λ_0 given by

$$\Lambda_0 = \frac{9\pi}{32} \frac{\mu_m d_0}{(\tau_s - \tau_d)} \quad (28)$$

for $m = II, III$, respectively mode II and mode III rupture; where $\mu_{II} = \mu$; $\mu_{III} = \mu/(1-\nu)$, with ν as the Poisson's ratio. [14] also approximate solution for Λ at large propagation distances (for mode III crack problems) given by

$$\Lambda = \frac{9}{16} \left(\frac{\mu d_0}{\Delta\tau} \right)^2 L^{-1} \quad \text{for } L \gg L_0 \quad (29)$$

where $\Delta\tau = (\tau_0 - \tau_d)$ is the stress drop, τ_0 the initial stress, L propagation distance, and L_0 is half of the critical crack length for a 2D crack given by

$$L_0 = \frac{\mu d_0 (\tau_s - \tau_d)}{\pi \Delta\tau^2} \quad (30)$$

As pointed out by [14], the two estimates of the cohesive width are complementary. The Λ_0 estimate shows that regardless of the background stress or rupture propagation distances, the numerical resolution is already constrained by the choice of the frictional parameters and elastic bulk properties; and it provides a convenient upper bound for the cohesive zone size (it is an upper bound in the sense that any nonzero rupture speed would shrink this zone even further due to Lorentz contraction [14]).

As stated in [14] the Λ estimate attempts to incorporate the background stress level (through the stress drop $\Delta\tau$) and the reduction of the cohesive zone (Lorentz contraction) due to the increasing rupture speed for large propagation distances L .

To relate numerical accuracy to the degree to which the cohesive zone is resolved, the authors in [14] have expressed the grid-size dependence of the solution in terms of the dimensionless ratio N_c . Where N_c is the ratio of the width of the cohesive zone, Λ , to the grid interval Δx .

$$N_c = \Lambda / \Delta x \quad (31)$$

This ratio provides a non-dimensional characterization of the resolution of a given numerical solution. As discussed in [14], even though N_c is a local measure of resolution, because Λ varies as the rupture propagates, both the Λ_0 estimate from (28) and the Λ estimate (29) should give good initial guidance as to what kind of spatial resolution will be needed in dynamic rupture propagation problems. However, as pointed out by [14], one should not expect a perfect quantitative agreement, as the estimates are derived with a number of simplifying assumptions.

Numerical test

SCEC benchmark problem version 3

Here we present some results collected from the series of papers [14,15,16], in which we have solved a three-dimensional (3D) problem of spontaneous rupture propagation for a planar fault embedded in a uniform infinite elastic isotropic space, using different numerical methods of Finite Difference and Boundary Integral (BI). The formulation and parameters of the test case correspond to Version 3 of the Southern California Earthquake Center (SCEC) benchmark problem [46]. The problem geometry is shown in Figure 5.

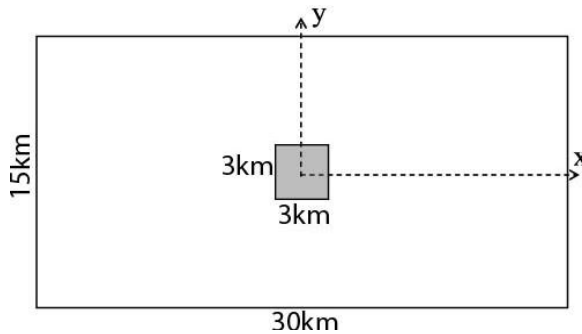


Figure 5. Fault geometry to test dynamic rupture simulation. The square in the center is the nucleation area where rupture initiates.

Table 1. Stress parameters for the numerical test of spontaneous dynamic rupture simulation.

Parameters	Within Fault Area of 30 km x 15km		Outside Fault Area
	Nucleation	Outside nucleation	
Initial shear stress (τ_0), MPa	81.6	70.0	70.0
Initial normal stress (σ_n), MPa	120.0	120.0	120.0
Static friction coefficient (μ_s)	0.677	0.677	infinite
Dynamic friction coefficient (μ_d)	0.525	0.525	0.525
Static yielding stress ($\tau_s = \mu_s \sigma_n$), MPa	81.24	81.24	infinite
Dynamic yielding stress ($\tau_d = \mu_d \sigma_n$), MPa	63.0	63.0	63.0
Dynamic stress drop ($\Delta\tau = \tau_0 - \tau_d$), MPa	18.6	7.0	7.0
Strength excess ($\tau_s - \tau_0$), MPa	-0.36	11.24	infinite
Critical slip distance, d_0 , m	0.40	0.40	0.40

We take the fault plane to be the x - y plane. The shear pre-stress is aligned with the x axis, and the origin of the coordinate system is located in the middle of the fault, as shown in Figure 5. The fault and pre-stress geometries are such that the x and y axes are axes of symmetry (or antisymmetry) for the fault slip and traction components. As a result, the xz plane undergoes purely in-plane motion, and the yz plane purely anti-plane motion.

Rupture is allowed within a fault area that extends 30 km in the x direction and 15 km in the y direction. A homogeneous medium is assumed, with a P wave velocity of 6000 m/s, S wave velocity of 3464 m/s, and density of 2670 kg/m³. The distributions of the initial stresses and frictional parameters on the fault are specified in Table 1.

Rupture nucleation

The rupture initiation of this kind of dynamic rupture problems is artificial and nucleation procedure can affect the rupture propagation (e.g. [47]). Here we adopt the criterion of overloading the initial stress at the nucleation patch, so rupture can initiate because the initial shear stress in the nucleation is set to be slightly (0.44%) higher than the initial static yield stress in that patch. Then the rupture propagates spontaneously through the fault area, following the linear slip-weakening fracture criterion (25). The nucleation size for the problem can be roughly estimated using equation (30) that give a value of $L_0 = 1.516$ km, which is half of the nucleation size. We assume that the nucleation shape is a square, so it will give a 3 km x 3 km square area centered on the fault, as shown in Figure 5.

Estimate of spatial resolution of the numerical model

As mentioned before, the cohesive zone developed during rupture propagation need to be accurately solved to obtain reliable solution of the problem. Then before simulation it is convenient to have some estimates of the degree of the numerical accuracy by calculating the spatial resolution to which the cohesive zone is resolved. For this purpose the approximate analytical cohesive zone Λ_0 from (28) and the Λ of (29) are calculated to estimate dimensionless ratio N_c of equation (31) as good initial guidance to define the spatial resolution needed for the test problem. Using the data of the test problem, we obtain zero-speed cohesive zone $\Lambda_0 = 620\text{m}$ for mode III, and $\Lambda_0 = 827\text{m}$ for mode II. They can be considered as the upper bound of our problem. The cohesive zone, Λ , at the maximum propagation distance $L=7.5\text{km}$ along the mode III is $\Lambda=251\text{m}$. Notice that the estimate of Λ for mode II cannot be derived analytically, it needs some numerical procedure not included in this work [14].

Assuming a grid size $\Delta x=100\text{m}$, the N_c value, from Eq. (31), is 6 to 8 for the upper bound, and 2.5 for the propagation distance. Those estimates indicate that a good spatial resolution for our problem requires $\Delta x \leq 100\text{m}$. The accuracy reached by this resolution will depend on the numerical method used to model the fault as well as the numerical technique used, as evaluated in [14,15,16].

Numerical techniques

The test problem is solved by two numerical techniques:

- 1) The so-called 3D dynamic fault model (DFM) code in which the TSN fault representation method is implemented [4,5,14, 48]. In the DFM the spatial difference operators are constructed by specializing trilinear elastic finite elements to the Cartesian mesh, approximating integrals by one-point quadrature, and diagonalizing the mass matrix (see more details of it in [14]). The method approximates temporal derivatives by explicit, central differencing in time. On a uniform mesh, the method is second-order accurate in space and time. In that case, the differencing scheme that results from this procedure is equivalent (away from the fault surface) to the second-order partly staggered grid method, which has been reviewed by [49] (see also in [50], p. 884, formula 25.3.22).
- 2) The 3D, four-order velocity-stress staggered (VSSG) wave propagation code of [51]. In this code we have implemented the SG and TSN fault representation method described earlier. The TSN formulation for the

VSSG FD scheme has been proposed by [16], as called by these authors, this implementation is referred to as the SGSN (staggered-grid split-node) method.

Numerical results

Numerical solutions for the DFM, SGSN and SG fault representations methods are briefly qualitatively discussed here. A complete quantitative and qualitative assessment of these methods and the solutions for this problem has been extensively discussed in our series of papers [14,15,16].

The highest grid resolution used for DFM, SGSN and SG methods are respectively 50m, 100m and 50m and referred respectively as DFM50, SGSN100 and SG50. The rupture arrival time (referred to as ‘‘rupture time’’ in the following) is a sensitive indicator of numerical precision, because this sensitivity reflects the nonlinearity of the problem. Relatively small inaccuracies in the calculated stress field can be expected to very significantly and affect the timing of rupture breakout from the nucleation zone as well as the subsequent rupture velocity. Therefore we have used rupture time differences as a primary means to show differences between our solutions. Figure 6 shows contours of rupture time for the three methods. The computed evolution of the rupture time is virtually identical for the DFM and SGSN solutions (Figure 6a), so that the contours for these two cases overlay and are nearly indistinguishable. The SG and DFM models (Figure 6b) have rupture contours that are very close together right after the initiation of the rupture, with differences increasing with the rupture propagation. As discussed in [15], rupture-time differences between SG and DFM cannot be accounted for by a simple time delay due to differences in nucleation, but

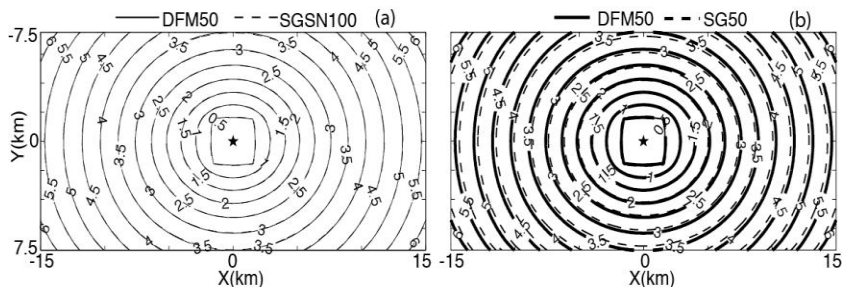


Figure 6. Contour plot of the rupture front for the dynamic rupture test problem: (a) comparison between DFM50 (grid size $\Delta x = 50\text{m}$) and SGSN100 ($\Delta x = 100\text{m}$) solutions; (b) comparison between DFM50 and SG50 ($\Delta x = 50\text{m}$) solutions.

represent systematic differences in rupture velocity over the entire rupture. Cohesive zone development for these methods along both x (inplane) and y (antiplane) axes are shown in Figure 7. DFM and SGSN are practically identical, the SG solutions produce a rupture with a cohesive-zone width that varies with propagation distance in a manner similar to the DFM and SGSN, but it is systematically narrower, but the cohesive-zone-width curves for the three methods have roughly the same shape. Qualitatively the three solutions provide comparable results. A relevant feature of the cohesive development is that as the crack velocity increases, the cohesive zone shrink in the direction of rupture propagation. This feature involves small-scale processes that need to be accurately solved, consequently it leads to numerical challenges in which calculations of such numerical simulations pose high demands in terms of required memory and processor power (e.g., [14]).

A quantitative estimation of the rupture time misfit as a function of grid interval for the three methods is shown in Figure 8. The rms misfits estimated in our papers [14,15,16] for the SG, DFM and SGSN methods use as reference solution the one calculated by the boundary integral (BI) method with grid size 100m presented in [14]. The BI method might provides

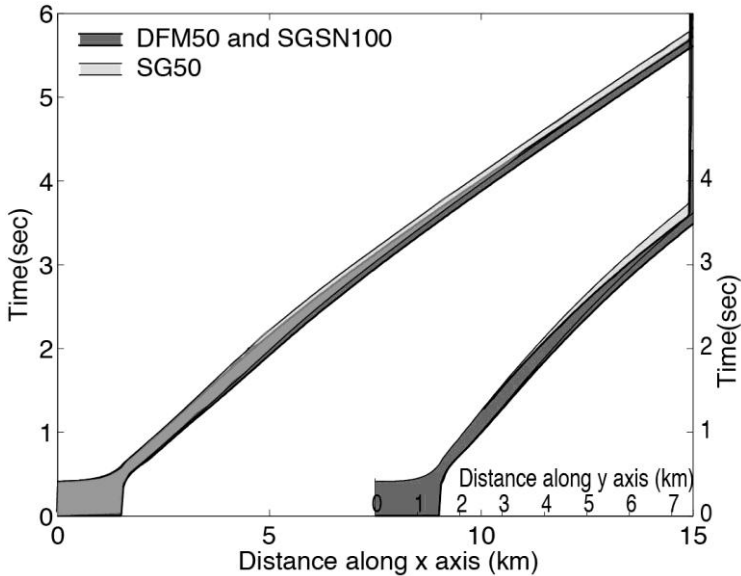


Figure 7. Cohesive zone evolution during rupture, along both inplane (x axis) and antiplane (y axis) directions for DFM50, SGSN100 and SG50.

semianalytical solutions for this problem, therefore it gives a suitable reference solution. The misfits of the DFM, SGSN and SG solutions as functions of Δx , or equivalently, as functions of resolution number N_c (Eq. 31) are shown in Figure 8. For reference, we also plot the results of the BI from [14].

As noted by [14], the DFM solutions follow a remarkably well-defined power law in the grid size, with exponent, or convergence rate, of approximately 3. DFM and BI methods share a nearly identical convergence rate and that both achieve misfits comparable. As presented by [16] the rupture-time differences for SGSN show a bilinear scaling with the grid size. The first scaling line corresponds to solutions with $\Delta x \leq 0.3$ and the second line for $\Delta x > 0.3$. The transition between these two scaling lines occurs between $\Delta x = 0.3$ and $\Delta x = 0.4$, corresponding to a grid interval slightly less

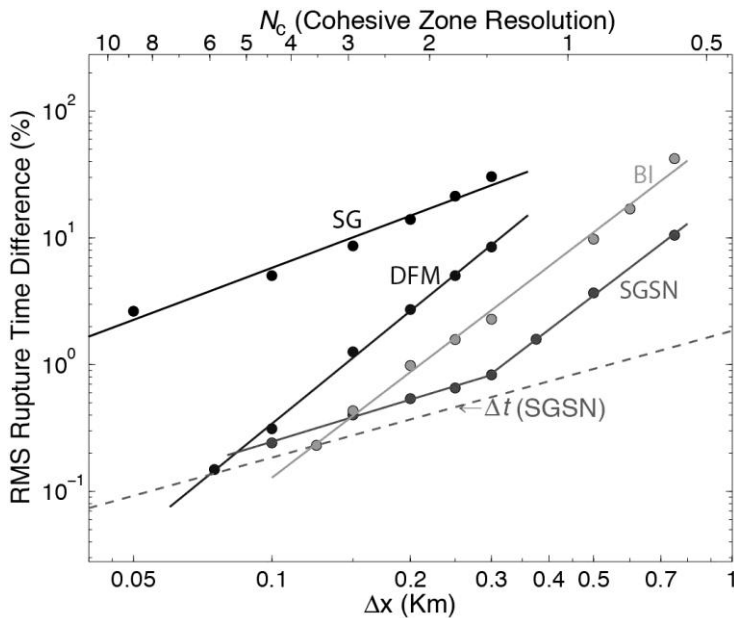


Figure 8. Misfit in time of rupture, relative to reference solution, shown as a function of grid interval Δx . Misfits are RMS averages over the fault plane for DFM, SGSN and SG solutions. All the solutions are relative to BI100m ($\Delta x=100\text{m}$) calculated by Day et al 2005. The dashed line shows the (approximate) dependence of time step Δt on Δx . The upper axis characterizes the calculations by their characteristic N_c values, where N_c is median cohesive zone width in the in-plane direction divided by Δx (Eq. 31).

than the median cohesive-zone width ($L = 0.44$ km) (see [16]). In the second line, for $\Delta x > 0.3$, the RMS time differences exceed 1.5% and the dependence upon Δx appears to follow a power law of exponent ~ 3 similar to the DFM and BI (see further discussion on it in [14,15,16]). But the SGSN has an exceptional performance. Very low misfit of order of $\sim 1\%$ is already achieved for $\Delta x = 0.3$, corresponding to $N_c \sim 1.5$. In contrast, the SG misfits follow a convergence rate with low power law of exponent ~ 1.4 , suggesting that this method is computational less efficient than the others.

A very insightful nature of this kind of dynamic rupture models is the rupture evolution that involves: initiation, evolution and stopping of the slip, and the evolution of the stress after the slipping ceases. So we reproduce the evaluation discussed in [14] of the slip rate and shear stress time history profiles along the x axis (in-plane direction) (Figure 9a) and the y axis (antiplane direction) (Figure 9b). We show results for the DFM50 only presented in [14]. For other solutions, SGSN100 and SG50, the feature discussed here are identical. As shown in these figures the pulses associated with the P and S waves returning from the borders of the fault are observed in the time histories of slip rate and stress. In Figures 9a and 9b we annotate these fault-edge-generated pulses. The P waves from the left and right borders of the fault traveling along the in-plane direction are denoted by ‘‘P’’ in Figure 9a. The pulses associated with the edge-generated S wave are indicated by ‘‘Si’’ and ‘‘Sa,’’ with Si corresponding to the pulses coming back from the left and right borders of the fault, traveling predominantly along the in-plane direction, and Sa corresponding to the pulses coming back from the top and bottom borders, traveling predominantly along the antiplane direction. In addition to these stopping phases, a late reactivation of slip, after its initial arrest, can also be seen in these figures. This feature is associated with the Si pulse, and its behavior is explained as follows. The P wave coming back from the boundary reduces the shear stress on the fault, causing slip to stop, leaving the shear stress somewhat below the dynamic friction value (dynamic overshoot). The subsequent Si fault edge pulse has to overcome that stress deficit in order to reinitiate slip. As it approaches the center of the fault, this pulse becomes weak. This wave experiences constructive interference at the center of the fault in which there is an encounter between the Si waves coming from the left and right side of the fault. As can be seen in the figures of shear stress, the Si pulse crosses the center and continues traveling to the other side of the fault, but always below the dynamic friction level, and therefore unable to produce further slipping.

Note that our solution procedure assumes, for simplicity, that once the dynamic frictional strength τ_d is reached at a point on the fault, the strength will

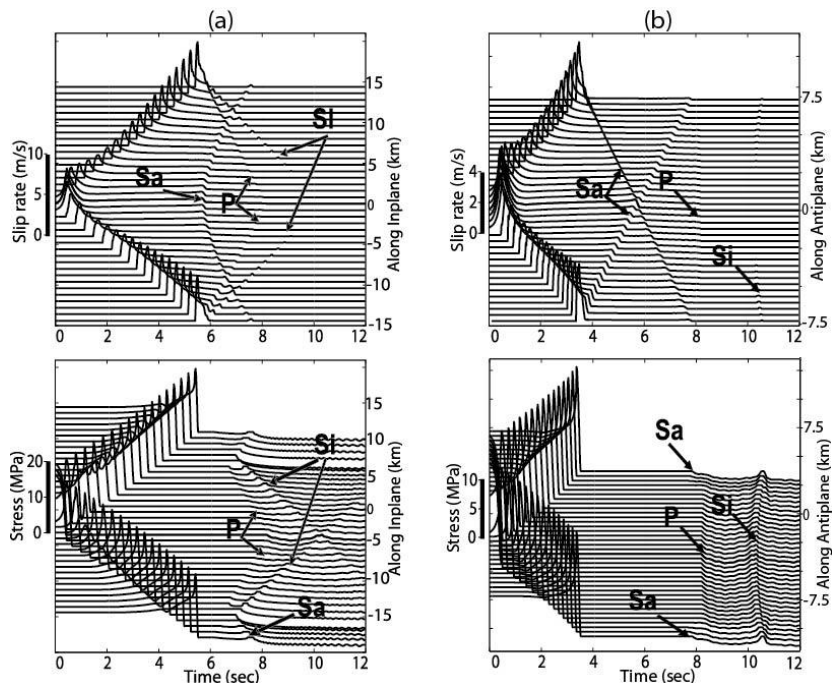


Figure 9. Time history of (top) slip rate and (bottom) shear stress for points along the axis of in-plane motion (x axis) (left) and antiplane motion (y axis) (right) for the DFM50 solution. The labels P and Si correspond to the P and S waves, respectively, generated at the left and right edges of the fault (i.e., propagating predominantly along the axis of in-plane motion). The label Sa identifies the S waves generated at the top and bottom of the fault (propagating predominantly along the antiplane axis).

not increase to larger values on the timescale of the computation, even if the point reaches zero slip velocity. That is, it is assumed that there is no healing for times of order of seconds. However, rock interfaces in the lab do exhibit healing at rest or small sliding velocities, and a more complete constitutive description would include that effect, but it is out of the scope of this work.

Large aspect-ratio fault ($L \gg W$)

One interesting application of dynamic rupture models is to study earthquake rupture in large aspect-ratio strike-slip faults with $L \gg W$, in which L and W are respectively the length and width of the fault. It is

expected that large earthquakes, such as the 2002 Mw 7.9 Denali and the 2008 Mw 8.0 Wenchuan earthquake in China, both with fault length about 300km, rupture the entire seismogenic thickness and are originated in large aspect-ratio faults. Therefore, the understanding of the rupture mechanism of this kind of fault is very important to address questions such as on why rupture extends so long, and what are the conditions to rupture stops before it becomes a large event.

Strike-slip faulting in a large aspect-ratio fault is dominated by the inplane rupture mode (mode II in fracture mechanics). Previous studies, such as from [4, 31] shows that in this kind of fault, the rupture is highly affected by the width (W). The main mechanism dominated in this kind of fault has been already explained in [4], that is, the fault initially ruptures as a crack-like (a simply-connected patch) around the hypocenter, but subsequently, at a time greater than that required for the rupture to cross the fault width, the rupture bifurcates into two separate pulses traveling in opposite directions due to the stopping phases coming from the top and bottom of the fault (see Figure 9 of the evolution of this stopping phases). When this process occurs in the bi-material case [31], it evolves interacting with the normal stress perturbation (characteristics of bimaterial fault rupture) and under very limited conditions it can lead to unilateral rupture (see details of this mechanism in [31]).

As complementary to the studies described above, here we model this kind of rupture problem to investigate the W effect on spontaneous rupture propagation in homogeneous strike slip faults. We fix the frictional parameters and nucleation rupture to be those of the SCEC benchmark problem, version 3, described in the previous section. Then we explore the sensitivity of rupture to variability of the fault width (W) in a fault with rupture propagation distance along strike of up to 400km. The grid size for these calculations is 50m.

Our results show that W takes an important role on rupture arresting and the generation of steady-state pulse-like rupture due to the arrival of the stopping phases (described in Figure 9) at the rupture front. Figures 10a,b,c shows respectively the rupture time, final slip and peak-slip rate along the inplane axis direction for different fault widths. Rupture is arrested for model with $W \leq 5.9$. For models larger than this width, the rupture propagation becomes self-sustained, increasing the rupture speed with increasing W .

Notice that rupture initiation for all the models is identical. All models reach the rupture speed limit (Rayleigh waves speeds) early, but then, when the rupture reaches the top and bottom of the fault, the ruptures speed, final

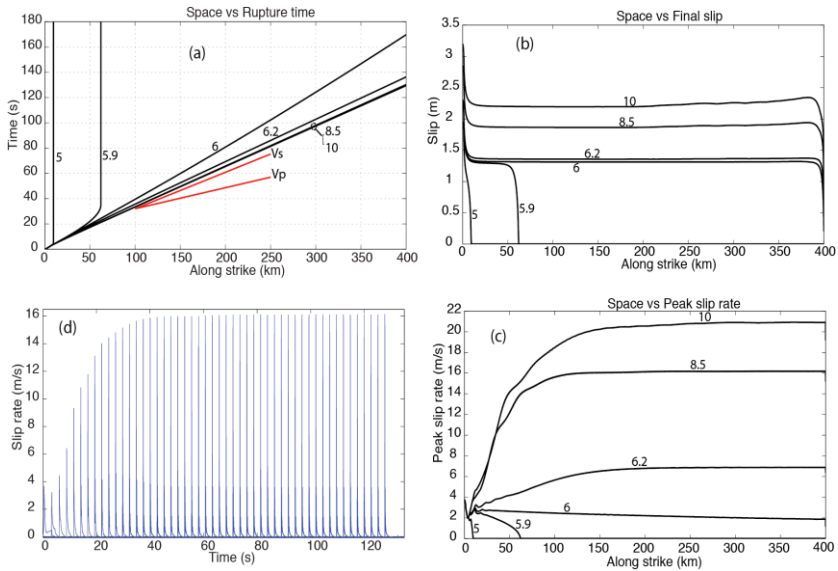


Figure 10. Rupture time (a), final slip (b) and peak slip rate (c) along the inplane axis of a strike slip fault with rupture propagation length of 400km, for different fault width (W). The number next to the line specifies the fault width. Figure (d) shows slip-rate vs time at each 8km interval along the inplane axis for the model with fault width $W=8.5$ km.

slip and peak slip rate are affected. Interesting, at rupture distance $L \gg W$ when the rupture is self-sustained, rupture propagates with a steady-state velocity pulse, i.e., the slip-rate pulse travels without altering its shape and amplitude, as shown in Figure 10d. This steady-state mechanism suggests that the cohesive zone length in the rupture front remains constant.

It is clear that the main mechanism dominating this kind of fault is due to the effect of stopping phases, as explained above. When this process occurs in a very narrow fault, the S-wave stopping phase reaches the rupture front early, and they are loaded with enough energy to arrest the rupture. But when the stopping phase reaches the rupture front late, the rupture front is already self-sustained, producing a complicated interaction between the stopping phase and the pulse dominated in the rupture front; consequently, the pulse becomes steady state.

From an energetic point of view, initially the fault is loaded with elastic energy that is dissipated during rupture propagation. The energy dissipated

during rupture increases with L , whereas the available elastic energy is proportional to W . For $L \gg W$, the dissipated energy becomes larger than the available elastic energy, leading to an eventual arresting of the rupture.

Remarks

Here we have described the numerical algorithms of two well known methods to represent fault discontinuity for spontaneous rupture dynamic calculation: the so-called traction at split-node (TSN) scheme and the inelastic-zone stress glut (SG) method. The main goal of this work is to introduce to the reader the conceptual implementation of these methods and its application in a simple test problem. For academic purpose, in appendix we provide the TSN implementation in a 1D wave equation that includes a matlab script, so the reader can follow the formulation and build his/her own code.

Advanced papers referred in Introduction are recommended to read for applications of these methods for different type of problems. There are recent development of fault representation and wave propagation technique not cited before, such as those used in Finite Volumes (FV) methods (e.g. [52,53]) and high order discontinues Galerkin (DG) methods (e.g. [54,55]). The nature of the fault representation in these methods is different than the TSN and SG method described here. The VF and DG incorporate formulations of fluxes to exchange information between the two surfaces of contact by solving the Riemann problem (e.g. [56]). These methods appear to be elegantly powerful and suitable to solve problems in extreme complex media and fault geometries. Another new generation algorithms emerging recently are the so-called adaptive mesh refinement formulations (e.g. [57]). Since rupture dynamic problems require to solve small scale in space and time during rupture propagation, these adaptive mesh algorithms appear to be the future application for this kind of problems.

Acknowledgments

The content of many part of this chapter has been published in our series of papers [14, 15 and 16] as specified in the text. Therefore I express my gratitude to the authors of these papers, Steven Day, Nadia Lapusta and Yi Liu. I also would like to thanks to Jean Paul Ampuero for enjoyable discussions on the last part of this chapter in which we discuss rupture dynamic on large aspect-ratio faults. Some of the simulations were done at the Swiss National Supercomputing Center (CSCS), under the production project "Development of Dynamic Rupture Models to Study the Physics of Earthquakes and Near-Source Ground Motion.

Appendix

Numerical implementation of the traction at split-node (TSN) fault representation in a 1D Elastodynamic equation for rupture dynamic problems

Let assume the fault plane is perpendicular to the z axis and located at $z=0$. To simplify the problem, we will implement the mixed boundary condition in a 1D wave equation, so all the fields depend only on z . This reduces to the condition that exactly the same thing is happening at every points along an infinitely fault plane.

Let use the velocity-stress form of the elastodynamic equations, in which the velocity $v(z,t)$ and shear stress $\tau(z,t)$ are the dependent variables:

$$\frac{\partial v}{\partial t} = \frac{1}{\rho} \frac{\partial \tau}{\partial z} \tag{A1}$$

$$\frac{\partial \tau}{\partial t} = \mu \frac{\partial v}{\partial z} \tag{A2}$$

Where μ is the shear module and ρ the density.

Let use the standard staggered grid finite difference for the spatial discretization of the equation (Figure A1). The fault normal is in the z direction and located at $z=0$. For simplicity, even un-realistic, we assume the existence of free-surface on the plus and minus domain of the discretization (see Fig. A1).

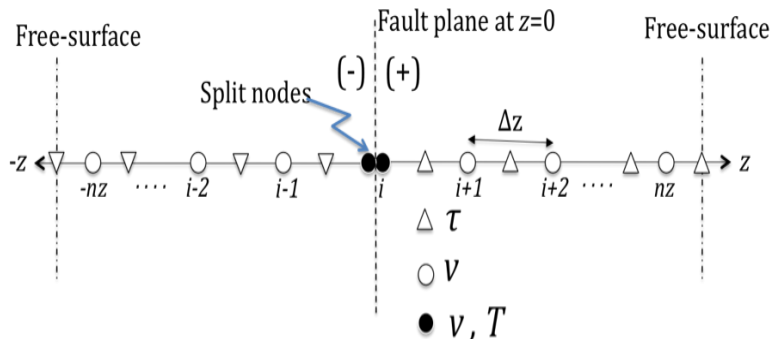


Figure A1. Staggered-grid discretization of the 1D elastodynamic equation with grid cells (split nodes) adjacent to the fault plane.

Approximation of spatial derivatives of equations A1 at the split nodes

Write separate equations for each side of the fault, taking into account the shear traction T acting at the interface, and its initial static equilibrium value T_0 . Introduce the following one-sided difference approximations for τ , applicable to the plus and minus sides of the fault, respectively.

$$\left(\frac{\partial \tau}{\partial z}\right)_i^\pm = \pm \frac{\tau_{i+1/2} - (T - T_0)_i^-}{0.5\Delta z} \quad [\text{A3}]$$

The time derivatives of equation (A1) at time t approximates by second-order central differences

$$\left(\frac{\partial v}{\partial t}\right)_i = \frac{v(t + \Delta t / 2) - v(t - \Delta t / 2)}{\Delta t} \quad [\text{A4}]$$

where Δt is the time step.

Approximation of spatial derivatives of equations A1 and A2 at interior grid points

Approximate the derivatives with a second-order spatial difference

$$\left(\frac{\partial \phi}{\partial z}\right)_i = \frac{\phi_{i+1/2} - \phi_{i-1/2}}{\Delta z} \quad [\text{A5}]$$

where ϕ represents an arbitrary stress τ or velocity component v

Approximation of free-surface boundary condition

Positioning the free-surface at the stress node (see figure A1), we satisfy the free-surface condition setting stress at this node to be zero

$$\begin{aligned} \tau_{nz+1/2} &= 0 \\ \tau_{-nz-1/2} &= 0 \end{aligned} \quad [\text{A6}]$$

Matlab script

Combining these equations (A1-A6) and the equations (5), (6), (11)-(15) on the fault described in the main text, we have wrote a matlab scripts at the end of this appendix. The matlab script is self explanatory. The example test

uses data assuming the fault is in the interface of two materials, plus side and minus side of the fault. The main feature modeled in this test are: 1) The test show evolution in time of slip velocity, slip and stress on the fault; 2) wave radiated from the fault toward the free-surface. Due to different material properties the test shows wave propagating at different speeds; 3) The effect of the free-surface on the radiated wave.

Data used in the matlab script test

Model geometry

$L = 5000\text{m}$; domain size (m) on each side of the fault

$\Delta z = 25\text{m}$; grid size

Material properties

$c^+ = 4000.0\text{ m/s}$; wave speed plus side of the fault

$\rho^+ = 2670.0\text{kg/m}^3$; density plus side of the fault

$\mu^+ = \rho^+(c^+)^2$ shear module plus side of the fault (Pa)

$c^- = 2000.0\text{ m/s}$; wave speed minus side of the fault

$\rho^- = 2670.0\text{kg/m}^3$; density minus side of the fault

$\mu^- = \rho^-(c^-)^2$ shear module minus side of the fault (Pa)

Friction and initial stress

$\sigma_n = 120\text{e}6\text{ Pa}$; initial normal stress on the fault

$\mu_s = 0.677$; static friction coefficient

$\mu_d = 0.525$; dynamic friction coefficient

$\tau_0 = 82.0\text{e}6\text{ Pa}$; initial shear stress

$d_0 = 0.4\text{ m}$; critical slip distance (m)

Simulation time

$t_{max} = 1.5 * L / c^+$;

Time discretization (CFL=0.5)

$dt = 0.5 * \Delta z / c^+$; time step

$nt = \text{integer}(tmax/dt)+1$; Number of time steps

Spatial discretization

$nz = \text{integer}(L/\Delta z)+1$; Number of grid points

Suggestions for other tests

You can play with the grid size to evaluate convergence and numerical oscillations. Use the same data above, but for $\Delta z = 10\text{m}, 50\text{m}, 100\text{m}, 200\text{m}, 400\text{m}$.

References

1. Andrews, D. J. 1976a, Rupture propagation with finite stress in antiplane strain, *J. Geophys. Res.* 81, 3575-3582.
2. Andrews, D. J. 1976b, Rupture velocity of plane-strain shear cracks, *J. Geophys. Res.* 81, 5679-5687.
3. Das, S., and K. Aki, Fault planes with barriers: A versatile earthquake model, *J. Geophys. Res.*, 82, 5648-5670.
4. Day, S. M. 1982a, Three-dimensional finite difference simulation of fault dynamics: rectangular faults with fixed rupture velocity, *Bull. Seismol. Soc. Am.*, 72, 705-727.
5. Day, S. M. 1982b, Three-dimensional simulation of spontaneous rupture: the effect of nonuniform prestress, *Bull. Seismol. Soc. Am.*, 72, 1881-1902.
6. Olsen, K. B., R. Madariaga, and R. Archuleta 1997, Three Dimensional Dynamic Simulation of the 1992 Landers Earthquake, *Science*. 278, 834-838.
7. Dalguer, L.A; Irikura K; Riera J. And Chiu H.C. 2001, The Importance of the Dynamic Source Effects on Strong Ground Motion During the 1999 Chi-Chi (Taiwan) Earthquake: Brief Interpretation of the Damage Distribution on Buildings. *Bull. Seismol. Soc. Am.*, 95, 1112-1127.
8. Dalguer, L.A; K. Irikura and J. Riera 2003a, Generation of New Cracks Accompanied by the Dynamic Shear Rupture Propagation of the 2000 Tottori (Japan) Earthquake, *Bull. Seismol. Soc. Am.*, 93, 2236-2252.
9. Dalguer, L.A., H. Miyake, S.M. Day and K. Irikura 2008, Surface Rupturing and Buried Dynamic Rupture Models Calibrated with Statistical Observations of Past Earthquakes. *Bull. Seismol. Soc. Am.* 98, 1147-1161, doi: 10.1785/0120070134.
10. Peyrat, S.; Olsen, K. and Madariaga, R. 2001, Dynamic modeling of the 1992 Landers earthquake, *J. Geophys. Res.* 106, 26,467-26,482

11. Oglesby, D. and Day, S.M. 2001, Fault Geometry and the Dynamics of the 1999 Chi-Chi (Taiwan) Earthquake. *Bull. Seismol. Soc. Am.*, 91, 1099-1111.
12. Aochi, H. and Fukuyama, E. 2002, Three-dimensional nonplanar simulation of the 1992 Landers earthquake. *J. Geophys. Res.*, 107, NO. B2, 2035, 10.1029/2000JB000061.
13. Olsen, K., S.M. Day, L.A. Dalguer, J. Mayhew, Y. Cui, J. Zhu, V.M. Cruz-Atienza, D. Roten, P. Maechling, T.H. Jordan, D. Okaya and A. Chourasia 2009, ShakeOut-D: Ground motion estimates using an ensemble of large earthquakes on the southern San Andreas fault with spontaneous rupture propagation, *Geophys. Res. Lett.*, 36, L04303, doi:10.1029/2008GL036832.
14. Day, S. M., L.A. Dalguer, N. Lapusta, and Y. Liu 2005, Comparison of finite difference and boundary integral solutions to three-dimensional spontaneous rupture, *J. Geophys. Res.*, 110, B12307, doi:10.1029/2005JB003813.
15. Dalguer, L. A., and S.M. Day 2006, Comparison of Fault Representation Methods in Finite Difference Simulations of Dynamic Rupture. *Bull. Seismol. Soc. Am.*, 96, 1764-1778.
16. Dalguer, L. A., and S.M. Day 2007, Staggered-Grid Split-Node Method for Spontaneous Rupture Simulation. *J. Geophys. Res.*, 112, B02302, doi:10.1029/2006JB004467.
17. Andrews, D. 1999, Test of two methods for faulting in finite-difference calculations, *Bull. Seism. Soc. Am.*, 89, 931-937.
18. Brietzke, G. B., A. Cochard, and H. Igel 2007, Dynamic rupture along bimaterial interfaces in 3D, *Geophys. Res. Lett.*, 34, L11305, doi:10.1029/2007GL029908.
19. Moczo, P., J. Kristek, M. Galis, P. Pazak, and M. Balazovjeh 2007, The finite-difference and finite-element modeling of seismic wave propagation and earthquake motion, *Acta physica slovacica*, 57(2), 177-406.
20. Oglesby, D., R. Archuleta, and S. Nielsen 1998, The three-dimensional dynamics of dipping faults, *Bull. Seism. Soc. Am.*, 90, 616-628.
21. Oglesby, D., R. Archuleta, and S. Nielsen 2000, Earthquakes on dipping faults: the effects of broken symmetry, *Science*, 280, 1055-1059.
22. Aagaard, B., T. Heaton, and J. Hall 2001, Dynamic earthquake rupture in the presence of lithostatic normal stresses: Implications for friction models and heat production, *Bull. Seism. Soc. Am.*, 91, 1765-1796.
23. Ma, S., S. Custodio, R. J. Archuleta, and P. Liu 2008, Dynamic modeling of the Mw 6.0 Parkfield, California, earthquake. *J. Geophys. Res.*, 113, B02301, doi:10.1029/2007JB005216.
24. Duan, B. 2010, Role of initial stress rotations in rupture dynamics and ground motion: A case study with implications for the Wenchuan earthquake. *J. Geophys. Res.*, 115, B05301, doi:10.1029/2009JB006750.
25. Galis, M., P. Moczo, and J. Kristek 2008, A 3-D hybrid finite-difference/finite-element viscoelastic modelling of seismic wave motion, *Geophys. J. Int.*, 175, 153-184.
26. Barall, M. 2010, Home of FAULTMOD Finite-Element Software, WWW.FAULTMOD.COM.

27. Vilotte, J.-P., G. Festa, and J.-P. Ampuero 2006, Dynamic fault rupture propagation using nonsmooth spectral element method, *Eos Trans. AGU*, 87(52), FallMeet. Suppl., Abstract S52B-05.
28. Kaneko, Y., N. Lapusta, and J.-P. Ampuero 2008, Spectral element modeling of spontaneous earthquake rupture on rate and state faults: Effect of velocity-strengthening friction at shallow depths, *J. Geophys. Res.*, 113, B09,317.
29. Galvez, P., J.-P. Ampuero, L. Dalguer, and T. Nissen-Meyer 2011, Dynamic rupture modeling of the 2011M9 Tohoku earthquake with unstructured 3D spectral element method, *Eos Trans. AGU*, 1(1), Fall Meet. Suppl., Abstract S24.
30. Day, S. M. 1991, Numerical simulation of fault propagation with interface separation (abstract), *Eos Trans. AGU*, 72, 486.
31. Dalguer, L. A. and S. M. Day 2009, Asymmetric Rupture of Large Aspect-ratio Faults at Bimaterial Interface in 3D. *Geophysical Research Letters*, 36, L23307, doi:10.1029/2009GL040303.
32. Ida, Y. 1972, Cohesive force across the tip of a longitudinal-shear crack and Griffith's specific surface energy, *J. Geophys. Res.*, 77, 3796-3805.
33. Palmer, A. C., and J. R. Rice 1973, The growth of slip surfaces in the progressive failure of overconsolidated clay slopes, *Proc. R. Soc. Lond.*, A332, 537.
34. Fukuyama E. and R. Madariaga 1998, Rupture dynamic of a planar fault in a 3D elastic medium: rate- and slip-weakening friction, *Bull. Seismol. Soc. Am.*, 88, 1-17.
35. Madariaga R., Olsen K., and Archuleta R. 1998, Modeling Dynamic Rupture in a 3D Earthquake Fault Model, *Bull. Seism. Soc. Am.* Vol. 88, 1182-1197.
36. Harris, R. A., and S. M. Day 1999, Dynamic 3D simulations of earthquakes on en echelon faults, *Geophys. Res. Letters*, 26, 2089-2092.
37. Dalguer, L.A; K. Irikura and J. Riera, 2003b, Simulation of Tensile Crack Generation by 3D Dynamic Shear Rupture Propagation During an Earthquake. *J. Geophys. Res.*, 108(B3), 2144, doi:10.1029/2001JB001738.
38. Dieterich, J.H. 1979, Modeling of rock friction, 1, Experimental results and constitutive equations. *J. Geophys. Res.*, vol. 84. pp. 2161-2168.
39. Ruina, A. 1983, Slip Instability and State Variable Friction Laws, *J. Geophys. Res.*, 88, 10359-10370.
40. Lachenbruch, A. H. 1980, Frictional heating, fluid pressure and the resistance to fault motion, *J. Geophys. Res.*, 85, 6097-6112.
41. Mase, C. W., and L. Smith 1985, Pore-fluid pressures and frictional heating on a fault surface, *Pure Appl. Geophys.*, 122, 583-607.
42. Mase, C. W., and L. Smith 1987, Effects of frictional heating on the thermal, hydrologic, and mechanical response of a fault, *J. Geophys. Res.*, 92, 6249-6272.
43. Rice, J. R. 2006, Heating and weakening of faults during earthquake slip, *J. Geophys. Res.*, 111(B5), B05311, doi: 10.1029/2005JB004006.
44. Barenblatt, G.I. 1959, The formation of equilibrium cracks during brittle fracture: General ideas and hypotheses, axially symmetric cracks, *Applied Mathematics and Mechanics (PMM)* 23, pp. 622-36.
45. Griffith, A. A. 1920, The phenomena of rupture and flow in solids, *Phil. Trans. Roy. Soc., Ser. A*, 221, 163-198.

46. Harris, R. A., M. Barall, R. Archuleta, E. M. Dunham, B. Aagaard, J. P. Ampuero, H. Bhat, V. Cruz-Atienza, L. Dalguer, P. Dawson, S. Day, B. Duan, G. Ely, Y. Kaneko, Y. Kase, N. Lapusta, Y. Liu, S. Ma, D. Oglesby, K. Olsen, A. Pitarka, S. Song, and E. Templeton 2009, The SCEC/USGS dynamic earthquake-rupture code verification exercise, *Seismological Research Letters*, 80(1), 119-126, doi:10.1785/gssrl.80.1.119.
47. Bizzarri, A. (2010), How to promote earthquake ruptures: Different nucleation strategies in a dynamic model with slip-weakening friction, *Bull. Seismol. Soc. Am.*, 100, 923-940, doi:10.1785/0120090179.
48. Day, S. M., and G. P. Ely 2002, Effect of a shallow weak zone on fault rupture: Numerical simulation of scale-model experiments, *Bull Seismol. Soc. Am.*, 92, 3022-3041.
49. Moczo, P., J. O. A. Robertsson, and L. Eisner 2007, The Finite-Difference Time-Domain Method for Modelling of Seismic Wave Propagation. In *Advances in Wave Propagation in Heterogeneous Earth*, 421-516, Wu, R.-S., Maupin, V., eds., *Advances in Geophysics* 48, Dmowska, R., ed., Elsevier – Academic Press, doi: 10.1016/S0065-2687(06)48008-0.
50. Abramowitz, M., and I. A. Stegun (1964), *Handbook of Mathematical Functions with Formulas, Graphs, and Mathematical Tables*, U.S. Dept. of Commer., Natl. Inst. of Stand. And Technol., Gaithersburg, Md., 1964.
51. Pitarka, A. 1999, 3D elastic finite-difference modeling of seismic motion using staggered grid with nonuniform spacing, *Bull. Seismol. Soc. Am.*, 89, 54-68.
52. Benjema, M., N. Glinsky-Olivier, V. Cruz-Atienza, J. Virieux, and S. Piperno 2007, Dynamic non-planar crack rupture by a finite volume method, *Geophys. J. Int.*, 171, 271-285.
53. Benjema, M., N. Glinsky-Olivier, V. Cruz-Atienza, and J. Virieux 2009, 3-D dynamic rupture simulations by a finite volume method, *Geophys. J. Int.*, 178, 541560, doi:10.1111/j.1365-246X.2009.04088.x.
54. de la Puente, J., J.-P. Ampuero, and M. Kaser 2009, Dynamic rupture modeling on unstructured meshes using a discontinuous Galerkin method, *J. Geophys. Res.*, 114, B10, 302, doi:10.1029/2008JB006271.
55. Pelties, C; J. de la Puente; J.-P. Ampuero; G. Brietzke and M. Kaser (2012) Three-dimensional dynamic rupture simulation with a high-order Discontinuous Galerkin method on unstructured tetrahedral meshes *J. Geophys. Res.*, 117, B02309, doi:10.1029/2011JB008857.
56. LeVeque, R. 2002, *Finite Volume Methods for Hyperbolic Problems*, Cambridge University Press, Cambridge.
57. Kozdon, J. E. and Dunham, E.M. 2011, Adaptive Mesh Refinement for Earthquake Rupture Simulations. 2011 SIAM Conference on Mathematical & Computational Issues in the Geosciences. MS19 Computational Challenges in Earthquake Simulation. March 21-24, 2011, Long Beach, CA.